CONFIDENTIAL. Limited circulation. For review only.

Ultra-Wideband Aided Inertial Navigation: Observability Analysis and Sensor Extrinsics Calibration

Abhishek Goudar, Karime Pereida and Angela P. Schoellig

***Abstract*— Inertial sensors aided by Ultra-wideband can provide accurate positioning in environments where Global Positioning Systems are unavailable. The positioning accuracy however, is contingent on accurate calibration of sensor extrinsics. This procedure is generally time consuming, requires specialized hardware and is prone to error. In this paper, we perform an observability analysis of the full state and sensor extrinsics. Based on this analysis we propose a method that simultaneously estimates system state and sensor extrinsics without any additional hardware or sensors using an indirect formulation of the Extended Kalman Filter. Experimental results demonstrate that the proposed method can estimate the sensor extrinsics to centimeter-level accuracy and estimate heading to milliradian-level accuracy.**

I. INTRODUCTION

The advent of Global Positioning System (GPS) revolutionzed positioning technology as the world moved from using map charts to using coordinates from handheld devices for navigation. Increased urbanization and industrialization has resulted in many economic activities moving to indoor environments such as factories, warehouses and shopping malls. Unfortunately, the performance of GPS degrades severly and in some cases is unavailable in indoor environments. This has warranted positioning systems similar to GPS but for indoor environments. The last few decades have seen the emergence of many different technologies as options for indoor positioning systems [1]. Ultra-wideband (UWB), on account of its high signal bandwith, general robustness to obstacles and long range, shows particular promise for accurate indoor localization [2], [3], [4].

A system equipped with a single UWB radio can estimate 3D position only. To obtain a full 6 degree-of-freedom (DOF) pose, inertial measurement units (IMU) are used in conjunction [4]. Additionally, one of the factors affecting UWB-based positioning systems is non-line-of-sight (NLOS) transmission. NLOS signals arise when the direct signal path is interrupted by physical objects resulting in longer transmission times. This is especially detrimental in applications requiring smooth and accurate tracking. The combination of IMU and UWB has been shown to imporve tracking performance in such applications [4].

Generally, IMU and UWB radios are not colocated. It is important to compensate for the sensor extrinsics or the lever-arm. This process is known as sensor extrinsic calibration. If uncalibrated, the offset will result in poor positioning performance. Current calibration techniques involve measuring the lever-arm manually, using specialized equipment, such as survey total station, or additional sensors. These methods are either prone to error or expensive. In this paper we first analyze the theoretical viability of estimating the sensor extrinsics between IMU and UWB using observability analysis. We then demonstrate experimentally the estimation of sensor extrinsics without additional hardware or sensors.

Moreover, in cases where a system has multiple UWB radios, the lever-arms can be used to estimate heading (within a local reference frame) without a magnetometer. Estimation of heading in this manner has many benefits. Unlike heading computed from integration of angular velocities from gyroscope data, the heading from multiple UWB radios is not susceptible to drift. Heading estimates from a magnetometer are vulnerable to interference from external magnetic fields. This can be problematic especially in factories and warehouses that have large metal structures and/or high voltage lines. On the contrary, heading computed from multiple UWB radios is unaffected in such conditions. Furthermore, this approach does not require any motion for aligning heading and thus enables true power-on-and-go systems.

In summary, the main contributions of this paper are:

1) We study the observability of the full state of an UWB-aided INS including the sensor extrinsics.
2) We estimate the full state and the sensor extrinsics using an indirect formulation of the Extended Kalman Filter (EKF) known as the Error State Kalman Filter (ESKF).
3) We show that accurate estimation of sensor extrinsics can be used to estimate heading in the presence of two or more mobile radios that are not co-located. We present experimental data that validates our approach.

In section II we review the most relevant works in literature. Section III provides the background material. Section IV and V provide a formal treatement of the problem. Section VI analyses the observability of the proposed system. An implementation of the ESKF as a realization of the system is presented in section VII. A discussion of the experimental results is presented in section VIII. Section IX concludes the paper.

II. RELATED WORK

Observability of combined visual and inertial sensor systems has been studied in [5], [6]. A similar treatement for visual-inertial navigation system (VINS) is provided in [7]. Observability of states in a multi-robot cooperative 2D localization setting is presented in [8] and [9].

The authors are with the Dynamic Systems Lab (http://www.dynsyslab.org), Institute for Aerospace Studies, University of Toronto, Canada, and affiliated with the Vector Institute for Artificial Intelligence in Toronto. E-mails: {name.lastname}@utoronto.ca

Manuscript 2104 submitted to 2020 IEEE/RSJ International Conference on Intelligent Robots and Systems. Received March 1, 2020.

The application of GPS in aiding INS has many parallels to UWB-aided INS as both GPS and UWB operate by estimating the time-of-flight. The effect of lever-arm and observability of GPS-aided INS has received much attention. The observability of piece-wise constant linear systems is presented in [10], [11]. The study of observability of simultaneous localization and mapping (SLAM) using GPS-aided INS is presented in [12]. The lever-arm however is not explicitly considered in this work. An explicit treatement of estimation of lever-arm is done in [13]. The observability of the error states under loosely coupled systems is studied which reduces the system and measurement models to linear functions and thus the linear matrix observability tests are used. In contrast, we consider a tightly coupled framework and study the obseravbility of the full non-linear model.

The use of UWB for indoor positioning has been demonstrated in the literature. A tightly coupled approach to localization using UWB and IMU is shown in [4] and [14]. The use of non-parametric estimation method, particle filter, for localization using UWB and wheel odometry is presented in [2]. An alternative to filtering-based methods employs graph optimization. UWB range measurements are treated as constraints on nodes of a graph and IMU measurements are used to generate relative pose constraints between nodes of a graph [3]. Other notable works which use different operating modes of UWB for positioning include [15] where wheel odometry is fused with time-difference-of-arrival (TDoA) measurements and [16] where only TDoA meausrements are used. However, none of these works treat the estimation of sensor extrinsics. An approach similar to the one followed in this paper is presented in [17]. However, in this case additional sensors such as cameras and GPS are used to estimate sensor extrinsics. To the best of the authors' knowledge, observability analysis of a tightly coupled UWB-aided INS for full 3D pose estimation including sensor extrinsics has not been done yet. Additionally, the estimation of magnetometer free heading using multiple UWB radios has does not have a precedence.

III. Background

In this section we introduce notation, methods and definitions used throughout the rest of the paper.

A. Differential Geometry and Non-Linear Observability

We provide a brief introduction to observability analysis of non-linear systems using a differential geometric approach as outlined in [18]. For a more rigorous treatement, we refer the reader to [19] and [18]. We introduce the following notation for the Lie derivative of a smooth function, $\mathbf{h}$ along a smooth vector field $\boldsymbol{f} : M \rightarrow TM$, where TM is the tangent bundle of the manifold M:

$$L_{\boldsymbol{f}}\mathbf{h}(\mathbf{x}) = \frac{\partial \mathbf{h}(\mathbf{x})}{\partial \mathbf{x}} \boldsymbol{f}(\mathbf{x}). \tag{1}$$

The corresponding gradient vector is denoted by:

$$\nabla L_{\boldsymbol{f}}\mathbf{h}(\mathbf{x}) = \left[\frac{\partial L_{\boldsymbol{f}}\mathbf{h}(\mathbf{x})}{\partial x_1}, ..., \frac{\partial L_{\boldsymbol{f}}\mathbf{h}(\mathbf{x})}{\partial x_n}, \right]. \tag{2}$$

Higher-order Lie derivatives are defined recursively as:

$$L^k_{\boldsymbol{f}}\mathbf{h}(\mathbf{x}) = \nabla L^{k-1}_{\boldsymbol{f}}\mathbf{h}(\mathbf{x})\boldsymbol{f}(\mathbf{x}),$$

with the zeroth-order Lie derviative defined as $L^0_{\boldsymbol{f}}\mathbf{h}(\mathbf{x}) = \mathbf{h}(\mathbf{x})$.

We consider causal non-linear systems that are affine in the control input:

$$\Sigma : \begin{cases} \dot{\mathbf{x}} = \boldsymbol{f}_0(\mathbf{x}) + \sum\limits_i \boldsymbol{f}_i(\mathbf{x}) u_i, \\ y = \mathbf{h}(\mathbf{x}), \end{cases} \tag{3}$$

where $u \in \Omega \subset \mathbb{R}^m$ and $\mathbf{x} \in M$, which is a smooth manifold of dimension n and $y \in \mathbb{R}^p$. The functions $\mathbf{f}_0$ and $\mathbf{f}_i$ are assumed to be smooth or as having derivatives of all orders in their domains denoted as C^∞. The observability test is based on the concept of *distinguishability* [18]. Two states $\mathbf{x}_0, \mathbf{x}_1 \in M$ are said to be *indistinguishable*, denoted $\mathbf{x}_0 I \mathbf{x}_1$, if the same input-output map is realized for every admissible input $u(t)$ for system Σ. This however does not imply that *every* combination of inputs can help distinguish between states in M. Instead, there might exist a combination of inputs that can distinguish between two states in M.

In this paper we focus on the concept of *local weak observablility*. The system Σ is locally weakly observable at $\mathbf{x}_0$ if there exists an open neighbourhood U in M of x_0 such that for every open neighbourhood V of $\mathbf{x}_0$ contained in U, the only point *indistinguishable* from $\mathbf{x}_0$ is $\mathbf{x}_0$, i.e. $I\{\mathbf{x}_0\} = \mathbf{x}_0$. Let $\mathcal{O}$ denote the matrix formed by stacking the gradients of Lie derivatives of the observation function $\mathbf{h}$. The system Σ is said to satisfy the *observability rank condition* if $\mathcal{O}$ is full rank. Furthermore, Σ is said to be locally weakly observable if it satisfies the observability rank condition.

B. Ultra-wideband

Common modes of operation of an UWB radio are: time-of-arrival (TOA), time-difference-of-arrival (TDoA) and two-way ranging (TWR). In TWR mode, the mobile radio actively pings the anchors in order to measure the distance. In constrast, in TOA and TDoA mode, the mobile radio passively listens to anchors and measures the arrival times from one or more anchors to localize. Operation in TOA and TDoA mode requires synchronization between clocks of anchors. In TDoA the performance outside the convex hull of anchors deterioates rapidly. In contrast, TWR mode does not require synchronization of clocks between the anchors and the performance deteriotes more slowly outside the convex hull of the anchors. For a more detailed survey of the scalability of TWR and TDoA we refer the reader to [20]. We use the TWR mode of operation in this paper.

We define some terms that will be used throughout the rest of the paper.

1) **anchor**, an UWB radio that is mounted in the surrounding environment. It is assumed that the position of anchor is known and fixed with respect to a local frame of reference. A collection of multiple anchors is referred to as a constellation.

Manuscript 2104 submitted to 2020 IEEE/RSJ International Conference on Intelligent Robots and Systems. Received March 1, 2020.

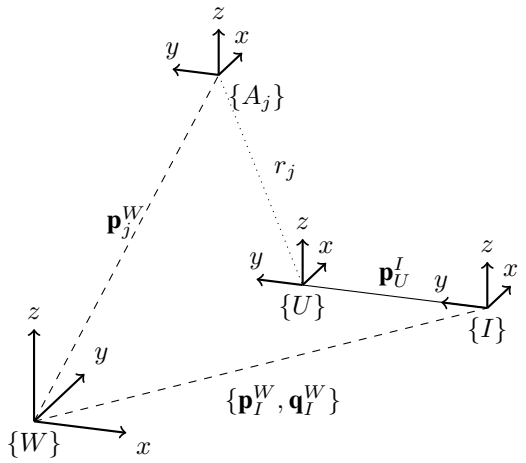

Fig. 1: The relationship between different frames involved in calibration of sensor extrinsics. Frame $\{W\}$ corresponds to a gravity-aligned world reference frame. IMU and mobile radio reference frames are represented by $\{I\}$ and $\{U\}$, respectively. The offset of mobile radio in the IMU frame is $\mathbf{p}_U^I$. The frame affixed to the phase center of j^{th} anchor is $\{A\}_j$ and its position in world reference frame is $\mathbf{p}_j^W$. The pose of the IMU in world frame is $\{\mathbf{p}_I^W, \mathbf{q}_I^W\}$.

2) **mobile radio**, an UWB radio mounted on a mobile system. In general, the mobile system can be any body that is to be tracked. Here, the mobile system corresponds to the sensor wand as shown in Figure 2.

Additionally, we define the following reference frames for this setup:

1) **mobile radio frame** $\{U\}$, a frame affixed to the phase center of the mobile radio antenna.
2) **IMU frame** $\{I\}$, frame corresponding to the IMU body center, in which the body accelerations and angular velocities are measured.
3) **world frame** $\{W\}$, a gravity-aligned absolute reference frame. The positions of individual anchors are expressed in this frame. The IMU is tracked with respect to this reference frame.
4) **anchor frame** $\{A\}_j$, a frame affixed to the phase center of the j^{th} anchor.

IV. Problem Formulation

In this work we estimate the sensor extrinsics between the mobile radio and the IMU along with relevant states. Further, in the presence of two or more mobile radios we exploit the lever-arms to compute drift-free heading without using a magnetometer. Simultaneous estimation of sensor extrinsics and relevant states precludes the need for a seperate calibration step thus enabling power-on-and-go systems. This also enables accurate localization in cases where the sensor positions change due to servicing, replacement or other activities.

Since the UWB radio is a point source, the orientation of the radio is irrelevant. Hence, the sensor extrinsics to be estimated reduces to the 3D position offset between the UWB radio and the IMU, henceforth also referred to as lever-arm. It is assumed that the mobile radio and IMU are mounted on a rigid body and therefore, the lever-arm is fixed and does not change over time. It is assumed that the mobile radio ranges to N_{anc} anchors in the constellation and that the position of the anchors is known with respect to the origin of a gravity-aligned reference frame.

V. System Modelling

1) System State: The system is parameterized by the following 19x1 state vector:

$$\mathbf{x}(t) = (\mathbf{p}_I^W(t), \mathbf{q}_I^W(t), \mathbf{v}_I^W(t), \mathbf{b}_a(t), \mathbf{b}_g(t), \mathbf{p}_U^I(t)), \quad (4)$$

where, $\mathbf{p}_I^W(t)$ is the position of the IMU in the world frame, $\mathbf{q}_I^W(t)$ is orientation of the IMU frame with respect to the world frame expressed as a unit quaternion, $\mathbf{v}_I^W(t)$ is the velocity of the IMU in the world frame, $\mathbf{b}_a(t)$ and $\mathbf{b}_g(t)$ are the IMU accelerometer and gyroscope biases, $\mathbf{p}_U^I(t)$ is the position of the mobile radio in the IMU frame. The first three terms constitute the core state and the last three terms correspond to the system parameters.

2) System Model: The system model adopted in this work is a 3D kinematic motion model similar to the one in [21], [22]. In this model the accelerometer measurements, $\boldsymbol{a}_m$, and gyroscope measurements, $\boldsymbol{\omega}_m$ are used as control inputs:

$$\dot{\mathbf{p}}_I^W = \mathbf{v}_I^W, \qquad \dot{\mathbf{q}}_I^W = \frac{1}{2}\mathbf{q}_I^W \otimes \boldsymbol{\omega}^m, \quad (5)$$

$$\dot{\mathbf{v}}_I^W = \mathbf{R}_I^W \boldsymbol{a}^m + \mathbf{g}^W, \qquad \dot{\mathbf{b}}_a = \mathbf{n}_{aw}, \quad (6)$$

$$\dot{\mathbf{b}}_g = \mathbf{n}_{gw}, \qquad \dot{\mathbf{p}}_U^I = \mathbf{0}_3, \quad (7)$$

where, $\mathbf{g}^W = [0, 0, 9.8]^T m/s^2$ represents the acceleration due to gravity in the world frame and $\mathbf{R}_I^W := \mathbf{R}\{\mathbf{q}_I^W\}$ is the direction cosine matrix (DCM) corresponding to the nominal orientation $\mathbf{q}_I^W$. The sensor models for accelerometer and gyroscopes are similar to [21], [22]. In this model the measurements are influenced by two terms: a high frequency noise term and a slowly varying bias term. The high frequency noise terms are modelled as zero-mean Gaussian white noise processes. The biases are modeled as Guassian random walk processes, driven by zero-mean Gaussian white noise process:

$$\boldsymbol{a}_m = \boldsymbol{a}^I + \mathbf{b}_a + \mathbf{n}_a, \quad (8)$$

$$\boldsymbol{\omega}_m = \boldsymbol{\omega}^I + \mathbf{b}_g + \mathbf{n}_g, \quad (9)$$

where, $\boldsymbol{a}^I$ and $\boldsymbol{\omega}^I$ denote the true linear acceleration and angular velocities expressed in body frame. The noise terms are represented by $\mathbf{n}_a$ and $\mathbf{n}_g$, with covariances $\mathbf{Q}_a$ and $\mathbf{Q}_g$ respectively i.e. $\mathbf{n}_a \sim \mathcal{N}(\mathbf{0}, \mathbf{Q}_a)$ and $\mathbf{n}_g \sim \mathcal{N}(\mathbf{0}, \mathbf{Q}_g)$. The biases $\mathbf{b}_a$ and $\mathbf{b}_g$ are driven by zero-mean Gaussian noise, $\mathbf{n}_{aw}$ and $\mathbf{n}_{gw}$, with covariances $\mathbf{Q}_{aw}$ and $\mathbf{Q}_{gw}$ respectively i.e. $\mathbf{n}_{aw} \sim \mathcal{N}(\mathbf{0}, \mathbf{Q}_{aw})$ and $\mathbf{n}_g \sim \mathcal{N}(\mathbf{0}, \mathbf{Q}_{gw})$.

3) Observation Model: A simple and tractable model is assumed for the UWB range measurements. In this model the measured distance between the j^{th} anchor $\mathbf{p}_j^W$ and mobile radio $\mathbf{p}_U^I$ is:

$$r_j = \|\mathbf{p}_j^W - \mathbf{p}_I^W \mathbf{R}_I^W - \mathbf{p}_U^I\|_2 + n_r, \quad (10)$$

where, $\|.\|_2$ denotes the l_2 norm or the euclidean norm and the meaurement error n_r is assumed to be a zero-mean Gaussian noise process, with covariance $\mathbf{Q}_r$ i.e. $n_r \sim \mathcal{N}(0, \mathbf{Q}_r)$.

Manuscript 2104 submitted to 2020 IEEE/RSJ International Conference on Intelligent Robots and Systems. Received March 1, 2020.

VI. Observability of Sensor Extrinsics

We study the observability of the full state, including the lever-arm, as defined in (4) under the observation model (10) by employing the *observability rank condition* as defined in section III-A. The system dynamics from (5)-(7) and (9) are rearranged to have a control affine form:

$$\dot{\mathbf{x}} = \underbrace{\begin{bmatrix} \mathbf{v}_I^W \\ -\mathbf{R}_I^W \mathbf{b}_a + \mathbf{g}^W \\ -\frac{1}{2}\boldsymbol{\Xi}\{\mathbf{q}_I^W\}\mathbf{b}_\omega \\ \mathbf{0}_3 \\ \mathbf{0}_3 \\ \mathbf{0}_3 \end{bmatrix}}_{f_0} + \underbrace{\begin{bmatrix} \mathbf{0}_{3\times3} \\ \mathbf{R}_I^W \\ \mathbf{0}_{3\times3} \\ \mathbf{0}_{3\times3} \\ \mathbf{0}_{3\times3} \\ \mathbf{0}_{3\times3} \end{bmatrix}}_{f_1} \mathbf{a}_m + \underbrace{\begin{bmatrix} \mathbf{0}_{3\times3} \\ \mathbf{0}_{3\times3} \\ \frac{1}{2}\boldsymbol{\Xi}\{\mathbf{q}_I^W\} \\ \mathbf{0}_{3\times3} \\ \mathbf{0}_{3\times3} \\ \mathbf{0}_{3\times3} \end{bmatrix}}_{f_2} \boldsymbol{\omega}_m, \tag{11}$$

where we omit the dependency on time for brevity and

$$\boldsymbol{\Xi}\{\mathbf{q}_I^W\} = \begin{bmatrix} q_1, & -q_2, & -q_3 \\ q_0, & -q_3, & q_2 \\ q_3, & q_0, & -q_1 \\ -q_2, & q_1, & q_0 \end{bmatrix}.$$

Without loss of generality, the measurement function (10) can be rewritten as:

$$h_1(\mathbf{x}) = \frac{1}{2}\|\mathbf{p}_j^W - \mathbf{R}_I^W \mathbf{p}_U^I - \mathbf{p}_I^W\|_2^2. \tag{12}$$

We consider measurements to $N_{anc} = 3$ *non-collinear* anchors i, j and k which results in the following measurement function:

$$\mathbf{h}_1(\mathbf{x}) = \frac{1}{2}\begin{bmatrix} \|\mathbf{p}_i^W - \mathbf{R}_I^W \mathbf{p}_U^I - \mathbf{p}_I^W\|_2^2 \\ \|\mathbf{p}_j^W - \mathbf{R}_I^W \mathbf{p}_U^I - \mathbf{p}_I^W\|_2^2 \\ \|\mathbf{p}_k^W - \mathbf{R}_I^W \mathbf{p}_U^I - \mathbf{p}_I^W\|_2^2 \end{bmatrix}. \tag{13}$$

For the system (11) to be locally weakly observable, the observability matrix $\mathcal{O}$ should have a rank of 19, which corresponds to the size of state (4). To this end we compute gradients of higher order Lie derivatives of the measurement function along the vector fields f_1, f_2 and f_3 to construct a rank 19 matrix. We start with the zeroth-order Lie derivative of $\mathbf{h}_1$ which is the function itself:

$$L^0\mathbf{h}_1(\mathbf{x}) = \mathbf{h}_1(\mathbf{x}). \tag{14}$$

The corresponding gradient is:

$$\nabla L^0\mathbf{h}_1(\mathbf{x}) = \big[-\delta\mathbf{p}_{ijk},\ \mathbf{0}_{3\times3}, -\delta\mathbf{p}_{ijk}\mathbf{F}_0,\ \mathbf{0}_{3\times3} \\ \mathbf{0}_{3\times3}, -\delta\mathbf{p}_{ijk}\mathbf{R}_I^W\big], \tag{15}$$

where $\mathbf{F}_0$ is a 3x4 matrix and is given by,

$$\mathbf{F}_0 = \frac{\partial\left(\mathbf{R}_I^W \mathbf{p}_U^I\right)}{\partial \mathbf{q}_I^W}, \tag{16}$$

and $\delta\mathbf{p}_{ijk} = [\delta\mathbf{p}_i^T, \delta\mathbf{p}_j^T, \delta\mathbf{p}_k^T]^T$ is a matrix of residuals with:

$$\begin{aligned} \delta\mathbf{p}_i &= \mathbf{p}_i^W - \mathbf{R}_I^W \mathbf{p}_U^I - \mathbf{p}_I^W, \\ \delta\mathbf{p}_j &= \mathbf{p}_j^W - \mathbf{R}_I^W \mathbf{p}_U^I - \mathbf{p}_I^W, \\ \delta\mathbf{p}_k &= \mathbf{p}_k^W - \mathbf{R}_I^W \mathbf{p}_U^I - \mathbf{p}_I^W. \end{aligned}$$

Now, we compute first order Lie derivatives. First, we consider the Lie derivative of $\mathbf{h}_1$ along the vector field f_0:

$$\begin{aligned} L_{f_0}^1\mathbf{h}_1(\mathbf{x}) &= \nabla L^0\mathbf{h}_1(\mathbf{x}) \cdot f_0 \\ &= \left[-\delta\mathbf{p}_{ijk}\mathbf{v}_I^W + \frac{1}{2}\delta\mathbf{p}_{ijk}\mathbf{F}_0\boldsymbol{\Xi}\{\mathbf{q}_I^W\}\mathbf{b}_\omega\right]. \end{aligned} \tag{17}$$

The gradient of $L_{f_0}^1\mathbf{h}_1(\mathbf{x})$ is:

$$\nabla L_{f_0}^1\mathbf{h}_1(\mathbf{x}) = \left[\mathbf{F}_1, -\delta\mathbf{p}_{ijk},\ \mathbf{F}_2,\ \mathbf{0}_{3\times3},\ \delta\mathbf{p}_{ijk}\mathbf{F}_3,\ \mathbf{F}_4\right]. \tag{18}$$

with $\mathbf{F}_1$, $\mathbf{F}_2$, $\mathbf{F}_3$ and $\mathbf{F}_4$ defined as:

$$\mathbf{F}_1 = \begin{bmatrix} \left(\mathbf{v}_I^W - \frac{1}{2}\mathbf{F}_0\boldsymbol{\Xi}\{\mathbf{q}_I^W\}\mathbf{b}_\omega\right)^T \\ \left(\mathbf{v}_I^W - \frac{1}{2}\mathbf{F}_0\boldsymbol{\Xi}\{\mathbf{q}_I^W\}\mathbf{b}_\omega\right)^T \\ \left(\mathbf{v}_I^W - \frac{1}{2}\mathbf{F}_0\boldsymbol{\Xi}\{\mathbf{q}_I^W\}\mathbf{b}_\omega\right)^T \end{bmatrix}, \tag{19}$$

$$\mathbf{F}_2 = \frac{\partial\{-\delta\mathbf{p}_{ijk}\mathbf{F}_1^T\}}{\partial \mathbf{q}_I^W}, \tag{20}$$

$$\mathbf{F}_3 = \frac{1}{2}\mathbf{F}_0\boldsymbol{\Xi}\{\mathbf{q}_I^W\}, \tag{21}$$

$$\mathbf{F}_4 = \frac{\partial\{-\delta\mathbf{p}_{ijk}\mathbf{F}_1^T\}}{\partial \mathbf{p}_U^I}. \tag{22}$$

We note that the first order Lie derivative of $\mathbf{h}_1$ along f_1 is identically zero and so we proceed to take the first order Lie derivative of $\mathbf{h}_1$ along f_2.

$$\begin{aligned} L_{f_2}^1\mathbf{h}_1(\mathbf{x}) &= \nabla L^0\mathbf{h}_1(\mathbf{x}) \cdot f_2 \\ &= \left[-\frac{1}{2}\delta\mathbf{p}_{ijk}\mathbf{F}_0\boldsymbol{\Xi}\{\mathbf{q}_I^W\}\right]. \end{aligned} \tag{23}$$

The matrix $L_{f_2}^1\mathbf{h}_1(\mathbf{x})$ is of dimension 3x3. We compute the gradient by stacking the gradients of individual columns to generate a 9x19 matrix:

$$\begin{aligned} \nabla L_{f_2}^1\mathbf{h}_1(\mathbf{x}) &= \begin{bmatrix} \nabla L_{f_2}^1\mathbf{h}_1(\mathbf{x})[:,1] \\ \nabla L_{f_2}^1\mathbf{h}_1(\mathbf{x})[:,2] \\ \nabla L_{f_2}^1\mathbf{h}_1(\mathbf{x})[:,3] \end{bmatrix} \\ &= \left[\mathbf{F}_5,\ \mathbf{0}_{9\times3},\ \mathbf{F}_6,\ \mathbf{0}_{9\times3},\ \mathbf{0}_{9\times3},\ \mathbf{F}_7\right], \end{aligned} \tag{24}$$

where, $\mathbf{F}_5$, $\mathbf{F}_6$, $\mathbf{F}_7$ are formed by stacking the the partial derivatives of individual columns of $L_{f_2}^1\mathbf{h}_1(\mathbf{x})$ with respect $\mathbf{p}_I^W, \mathbf{q}_I^W$ and $\mathbf{p}_U^I$ respectively.

Now, we compute the second order Lie derivatives. We first consider the second order Lie derivative of $\mathbf{h}_1$ along f_0. This can be computed recursively:

$$\begin{aligned} L_{f_0}^2\mathbf{h}_1(\mathbf{x}) &= \nabla L^1\mathbf{h}_1(\mathbf{x}) \cdot f_0 \\ &= \Big[\mathbf{F}_1\mathbf{v}_I^W + \delta\mathbf{p}_{ijk}\left(\mathbf{R}_I^W\mathbf{b}_a + \mathbf{g}^W\right) \\ &\quad - \frac{1}{2}\mathbf{F}_2\boldsymbol{\Xi}\{\mathbf{q}_I^W\}\mathbf{b}_\omega\Big], \end{aligned} \tag{25}$$

The gradient of $L_{f_0}^2\mathbf{h}_1(\mathbf{x})$ is:

$$\nabla L_{f_0}^2\mathbf{h}_1(\mathbf{x}) = [\mathbf{F}_8,\ \mathbf{F}_9,\ \mathbf{F}_{10},\ \delta\mathbf{p}_{ijk}\mathbf{R}_I^W,\ \mathbf{F}_{11},\ \mathbf{F}_{12}]. \tag{26}$$

Manuscript 2104 submitted to 2020 IEEE/RSJ International Conference on Intelligent Robots and Systems. Received March 1, 2020.

$$\mathcal{O} = \begin{bmatrix} \nabla L^0 \mathbf{h}_1 \\ \nabla L^1_{f_0} \mathbf{h}_1 \\ \nabla L^1_{f_2} \mathbf{h}_1 \\ \nabla L^2_{f_0} \mathbf{h}_1 \\ \nabla L^1_{f_2} L^1_{f_0} \mathbf{h}_1 \end{bmatrix} = \begin{bmatrix} -\delta \mathbf{p}_{ijk} & \mathbf{0}_{3\times3} & -\delta \mathbf{p}_{ijk}\mathbf{F}_0 & \mathbf{0}_{3\times3} & \mathbf{0}_{3\times3} & -\delta \mathbf{p}_{ijk}\mathbf{R}_I^W \\ \mathbf{F}_1 & -\delta \mathbf{p}_{ijk} & \mathbf{F}_2 & \mathbf{0}_{3\times3} & \delta \mathbf{p}_{ijk}\mathbf{F}_3 & \mathbf{F}_4 \\ \mathbf{F}_5 & \mathbf{0}_{9\times3} & \mathbf{F}_6 & \mathbf{0}_{9\times3} & \mathbf{0}_{9\times3} & \mathbf{F}_7 \\ \mathbf{F}_8 & \mathbf{F}_9 & \mathbf{F}_{10} & \delta \mathbf{p}_{ijk}\mathbf{R}_I^W & \mathbf{F}_{11} & \mathbf{F}_{12} \\ \mathbf{F}_{13} & \mathbf{F}_{14} & \mathbf{F}_{15} & \mathbf{0}_{9\times3} & \mathbf{F}_{16} & \mathbf{F}_{17} \end{bmatrix}, \tag{29}$$

Finally, we compute the the Lie derivative of $L^1_{f_0}$ along the vector field f_2:

$$L^1_{f_2} L^1_{f_0} \mathbf{h}_1(\mathbf{x}) = \nabla L^1_{f_0} \mathbf{h}_1(\mathbf{x}) \cdot f_2 = \left[\frac{1}{2} \mathbf{F}_2 \Xi\{\mathbf{q}_I^W\} \right], \tag{27}$$

which is a 3x3 matrix. As before, we compute the gradient by stacking the gradients of individual columns:

$$\begin{aligned} \nabla L^1_{f_2} L^1_{f_0} \mathbf{h}_1(\mathbf{x}) &= \begin{bmatrix} \nabla L^1_{f_2} L^1_{f_0} \mathbf{h}_1(\mathbf{x})[:,1] \\ \nabla L^1_{f_2} L^1_{f_0} \mathbf{h}_1(\mathbf{x})[:,2] \\ \nabla L^1_{f_2} L^1_{f_0} \mathbf{h}_1(\mathbf{x})[:,3] \end{bmatrix} \\ &= \begin{bmatrix} \mathbf{F}_{13}, & \mathbf{F}_{14}, & \mathbf{F}_{15}, & \mathbf{0}_{9\times3}, & \mathbf{F}_{16}, & \mathbf{F}_{17} \end{bmatrix}. \end{aligned} \tag{28}$$

Stacking the gradients of the zeroth order, first order and second order Lie derivatives, we obtain a matrix of dimension 27x19 as shown in (29). Note that addition of Lie derivatives of higher order will not affect the rank of the matrix $\mathcal{O}$. If the matrix as defined by (29) is full rank, then the state (4) is locally weakly observable.

Given the dense nature of the observability matrix, block Gaussian elimination cannot be applied to determine the rank of the matrix. Instead, we perform a rank test on the symbolic matrix. Recall that the rank of a submatrix is always less than or equal to the rank of the original matrix and so it suffices to test the ranks of submatrices of increasing dimension. To that effect, we perform a rank test on the matrix $\mathcal{O}_s$ which is of dimension 21x19 using Mathematica [1]. The matrix $\mathcal{O}_s$ is obtained by dropping the bottom 6 rows from $\mathcal{O}$. The symbolic rank test reveals that $\mathcal{O}_s$ is full rank suggesting that the system is locally weakly observable with range measurements to three non-collinear anchors.

VII. Error-State Kalman Filter

The analysis in the previous section sugges that the full state is observable. We use the ESKF [21], [22] to estimate the sensor extrinsics and the core state simultaneously. In this formulation, inertial navigation based dead reckoning is used to propogate the state forward using the model (3) and IMU measurements as control inputs. The associated uncertainity is estimated in the prediction step of the ESKF. Since the accelerometer and gyroscope measurements are used as control inputs, the system noise covariance matrix, $\mathbf{Q}_p$, for the prediction step is generated from the covariances of the noise and bias terms as defined in section V and (9). Concretely, $\mathbf{Q}_p = \text{diag}\left(\mathbf{Q}_a, \mathbf{Q}_g, \mathbf{Q}_{aw}, \mathbf{Q}_{gw}\right)$. Upon receipt of UWB range measurements the correction step of the ESKF is triggered. During this step the error between the dead reckoned state and the state consistent with range measurements is estimated. The estimated error state is:

$$\delta \mathbf{x} = (\delta \mathbf{p}_I^W, \delta \mathbf{v}_I^W, \delta \boldsymbol{\theta}_I^W, \delta \mathbf{b}_a, \delta \mathbf{b}_\omega, \delta \mathbf{p}_U^I), \tag{30}$$

where, $\delta \mathbf{p}_I^W$ represents the error between dead reckoned position and the position consistent with range measurements. A similar interpretation holds for other error states. The angular error $\delta \boldsymbol{\theta}_I^W$ is related to small differential rotations $\delta \mathbf{q}_I^W$ as:

$$\delta \mathbf{q} = \begin{bmatrix} 1 \\ \delta \boldsymbol{\theta} \end{bmatrix}, |\delta \boldsymbol{\theta}| \ll 1. \tag{31}$$

The estimated error state is then added to the dead reckoned state to compensate for accumulated error on account of drift:

$$\mathbf{x} = \mathbf{x} \otimes \delta \mathbf{x}, \tag{32}$$

where $\otimes$ is a generic composition operator that refers to quaternion multiplication for orientation error and addition for other error states. We refer the reader to [22] for a thorough description of the ESKF prediction and correction steps.

VIII. Experiments and Discussion

A. Experimental Setup

In this section we present the setup used in the experiments. The setup consists of a sensor wand, a constellation of 6 anchors and a motion capture system. The sensor wand is equipped with an Xsens IMU and two Decawave UWB radios mounted as shown in Figure 2. The IMU outputs linear accelerations and angular velocities at 100Hz. Range measurements are acquired at 18Hz (9Hz for individual mobile radio) by pinging the individual anchors. The position of anchors in the constellation is measured manually using a survey Total Station. The IMU and UWB range measurements are then input into an ESKF that estimates the core state as well as the lever-arms between both the

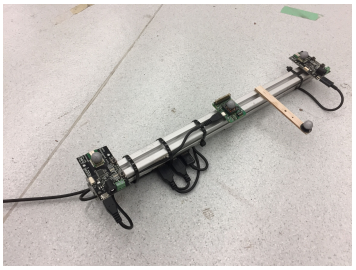

Fig. 2: The sensor apparatus consists of a wand equppied with an Xsens IMU mounted in the middle. Two UWB mobile radios are mounted on the left and right side of the IMU respectively. Reflective markers are mounted purely for evaluation against ground truth.

[1] http://tiny.cc/k6iqkz

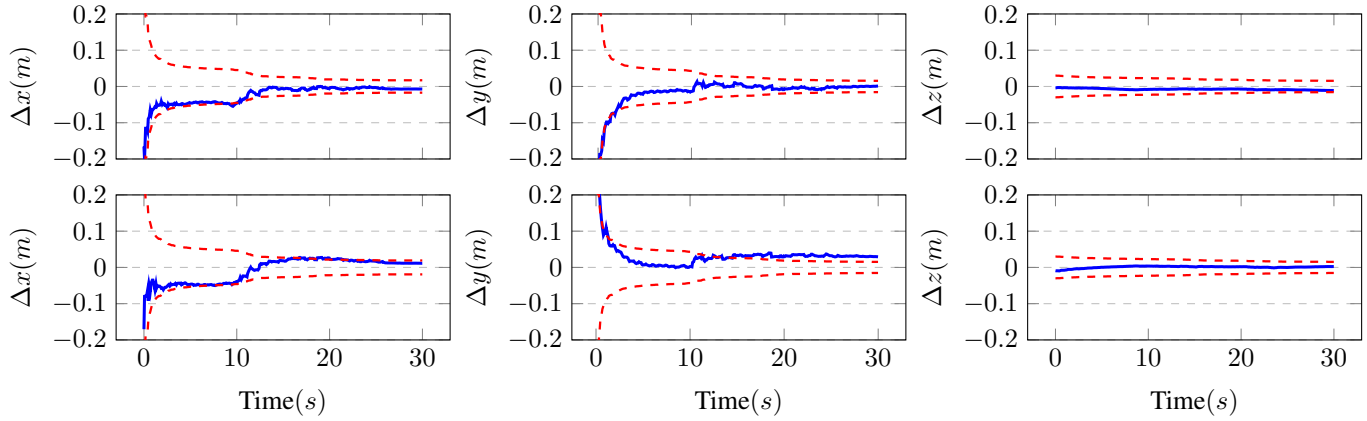

Fig. 3: Sensor extrinsic estimation error with corresponding 3σ covariance bounds for Trial #1. Δx, Δy and Δz denote residual error between the estimated mobile radio position and the ground truth, along x,y and z axis respectively. Error plots for the left mobile radio are shown in the first row and error plots for the right mobile radio are shown in the second row.

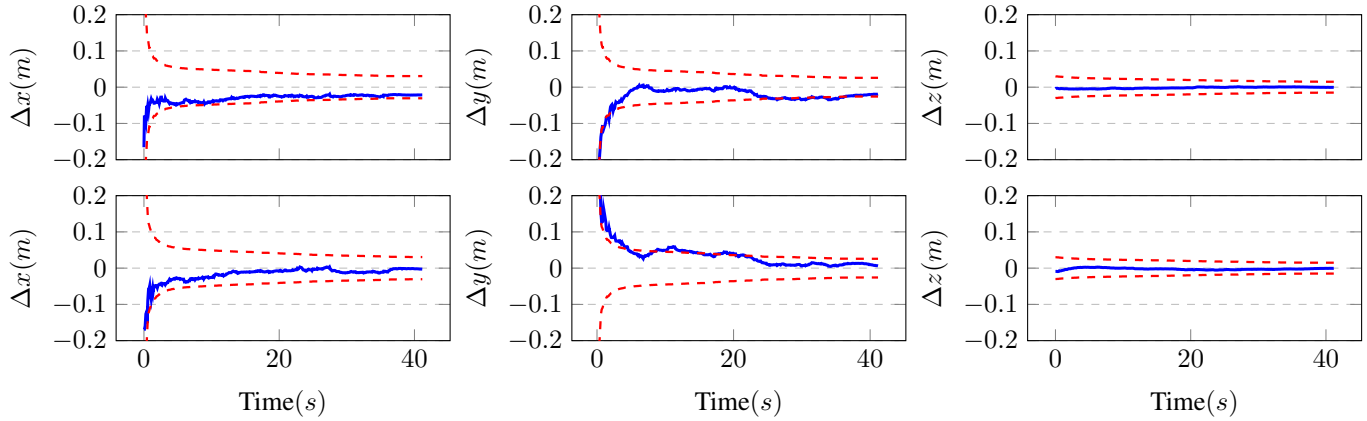

Fig. 4: Sensor extrinsic estimation error with corresponding 3σ covariance bounds for Trial #2. Δx, Δy and Δz denote residual error between the estimated mobile radio position and the ground truth, along x,y and z axis respectively. Error plots for the left mobile radio are shown in the first row and error plots for the right mobile radio are shown in the second row.

mobile radios and the IMU. Reflective markers mounted on the IMU and the mobile radios are used to acquire ground truth pose information of the wand from the motion capture system (at 300Hz) as it moves through the constellation. The Decawave UWB modules used in this experiment claim a range precision of $\pm$10cm.

B. Experimental Results

We performed multiple experiments to mainly test *1)* estimation accuracy of the lever-arm, and *2)* heading estimation using multiple radios. In all of the experiments the sensor wand was moved manually in different trajectories.

TABLE I: Residual error in estimation of sensor extinsics along the body x, y and z axis shown as $\Delta x, \Delta y$ and Δz respectively. The corresponding 3σ bounds are plotted as well.

	Left Mobile Radio		Right Mobile Radio	
Error (cm)	Trial #1	Trial #2	Trial #1	Trial #2
$\Delta x \pm 3\sigma$	-0.3±0.6	1.1±1.0	-2.14±0.6	-0.72±1.1
$\Delta y \pm 3\sigma$	-0.2±0.5	1.9±0.9	-2.9±0.5	-0.6±0.9
$\Delta z \pm 3\sigma$	1.1±0.5	0.07±0.5	-0.3±0.5	-0.03±0.5
RMSE	1.2	2.2	3.6	0.9

1) Lever-arm Estimation: Results of lever-arm estimation are shown in Table I including the root-mean-square error (RMSE) for two experiments. The corresponding error plots are shown in Figure 3 and 4. The vector $(\Delta x,\ \Delta y,\ \Delta z)$ represents the error between the estimated lever-arm and the ground truth position of the mobile radios. The corresponding covariance estimates are obtained from the process covariance matrix of the ESKF.

The initial error in both the lever-arms was $\sim (\Delta x = 0.16m, \Delta y = 0.30m, \Delta z = 0.1m)$. The results show that the lever-arms are estimated to within centimeter to sub-centimeter level accuracy with sufficient excitation along all the axis within 30-40 seconds. This shows that it is possible to estimate lever-arm using just an IMU and an UWB radio without additional hardware.

2) Heading Estimation with Multiple UWB Modules: Errors in estimation of position and orientation are presented in Table II. The position error vector $(\Delta p_x, \Delta p_y, \Delta p_z)$ represents the difference between the estimated position $\mathbf{p}_I^W$ of

TABLE II: Position and orientation error of the IMU in the world frame with 3σ covariance bounds. The mean position error $(\Delta p_x, \Delta p_y, \Delta p_z)$ is the difference between the estimated position $\mathbf{p}_I^W$ and the corresponding ground truth in the world frame. The orientation error vector $(\Delta\theta, \Delta\phi, \Delta\psi)$ represents the mean roll, pitch and yaw error between the estimated orientation $\mathbf{q}_I^W$ and the ground truth orientation.

Position Error(m)	Trial #1	Trial #2	Orientation Error(rad)	Trial #1	Trial #2
$\Delta p_x \pm 3\sigma$	0.051 $\pm$ 0.229	-0.003 $\pm$ 0.328	$\Delta\phi \pm 3\sigma$	0.007 $\pm$ 0.162	0.008 $\pm$ 0.177
$\Delta p_y \pm 3\sigma$	0.013 $\pm$ 0.243	-0.019 $\pm$ 0.352	$\Delta\theta \pm 3\sigma$	0.002 $\pm$ 0.055	-0.0051 $\pm$ 0.105
$\Delta p_z \pm 3\sigma$	-0.015 $\pm$ 0.309	-0.109 $\pm$ 0.307	$\Delta\psi \pm 3\sigma$	-0.034 $\pm$ 0.186	-0.066 $\pm$ 0.1401

the IMU and the corresponding ground truth. The orientation error vector $(\Delta\theta, \Delta\phi, \Delta\psi)$ represents the mean roll, pitch and yaw error between the estimated orientation $\mathbf{q}_I^W$ and ground truth. We focus on heading estimation in this work. In all of the experiments the wand was held static for an initial period of 10 seconds. Without heading from multiple modules, the heading drifts on account of dead-reckoning. However, it can be seen from Table II that with multiple mobile radios, this is not the case. This suggests that drift-free heading can be estimated in the presence of multiple non-colocated mobile radios.

C. Discussion

The analysis presented in this work is applicable to systems equipped with any number of mobile radios as the estimation of lever-arm for an individual radio is done independent of other radios. Furthermore, while the analysis presented here is specific to UWB measurements, the proposed approach is agnostic to UWB sensors and is applicable to any sensor that provides point-to-point range measurements.

IX. Conclusion and Future Work

In this work we analyzed the observability of core state and lever-arm for UWB-aided inertial navigation systems. Both, the analysis and the experiments show that online calibration of the lever-arm can be achieved without using any additional hardware or equipment and using only the available sensors. Also, the estimated sensor extrinsics can be exploited to estimate precise heading in the local reference frame thus enabling power-on-and-go localization.

One of the factors limiting the estimation accuracy is the precision of the measurements. Another contributing factor is any uncompensated bias that accomponies the measurement. This may arise due to various factors such as incorrect anchor locations or inherent bias in the mobile radio. As a part of the future work, we aim to estimate the biases in anchor locations and the biases inherent in the mobile radio to achieve better performance.

References

[1] Faheem Zafari, Athanasios Gkelias, and Kin K. Leung. A Survey of Indoor Localization Systems and Technologies. *IEEE Communications Surveys and Tutorials*, 21(3):2568–2599, 2019.

[2] Amanda Prorok and Alcherio Martinoli. Accurate indoor localization with ultra-wideband using spatial models and collaboration. *International Journal of Robotics Research*, 33(4):547–568, 2014.

[3] Xu Fang, Chen Wang, Thien-Minh Nguyen, and Lihua Xie. Graph optimization approach to localization with range measurements. *arXiv preprint arXiv:1802.10276*, 2018.

[4] J. D. Hol, F. Dijkstra, H. Luinge, and T. B. Schon. Tightly coupled UWB/IMU pose estimation. In *Proc. of the IEEE International Conference on Ultra-Wideband*, pages 688–692, 2009.

[5] Visual-inertial sensor fusion: Localization, mapping and sensor-to-sensor Self-calibration. *International Journal of Robotics Research*, 30(1):56–79, 2011.

[6] Stephan M Weiss. *Vision based navigation for micro helicopters*. PhD thesis, ETH Zurich, 2012.

[7] Joel A. Hesch, Dimitrios G. Kottas, Sean L. Bowman, and Stergios I. Roumeliotis. Camera-IMU-based localization: Observability analysis and consistency improvement. *International Journal of Robotics Research*, 33(1):182–201, 2014.

[8] Brandon Araki, Igor Gilitschenski, Tatum Ogata, Alex Wallar, Wilko Schwarting, Zareen Choudhury, Sertac Karaman, and Daniela Rus. Range-based cooperative localization with nonlinear observability analysis. In *Proc. of the IEEE Intelligent Transportation Systems Conference (ITSC)*, pages pp. 1894–1870, 2019.

[9] Qin Shi, Xiaowei Cui, Sihao Zhao, Jian Wen, and Ming quan Lu. Range-only collaborative localization for ground vehicles. *ArXiv*, abs/1912.01182, 2019.

[10] D. Goshen-Meskin and I. Y. Bar-Itzhack. Observability analysis of piece-wise constant systems. I. Theory. *IEEE Transactions on Aerospace and Electronic Systems*, 28, 1992.

[11] D. Goshen-Meskin and I. Y. Bar-Itzhack. Observability analysis of piece-wise constant systems. II. Application to inertial navigation in-flight alignment (military applications). *IEEE Transactions on Aerospace and Electronic Systems*, 28, 1992.

[12] M. Bryson and S. Sukkarieh. Observability analysis and active control for airborne slam. *IEEE Transactions on Aerospace and Electronic Systems*, 44(1):261–280, January 2008.

[13] Sinpyo Hong, Man Hyung Lee, Ho-Hwan Chun, Sun-Hong Kwon, and J. L. Speyer. Observability of error States in GPS/INS integration. *IEEE Transactions on Vehicular Technology*, 54(2):731–743, March 2005.

[14] Mark W. Mueller, Michael Hamer, and Raffaello D'Andrea. Fusing ultra-wideband range measurements with accelerometers and rate gyroscopes for quadrocopter state estimation. In *Proc. of the IEEE International Conference on Robotics and Automation (ICRA)*, pages 1–6, 2015.

[15] Amanda Prorok, Phillip Tomé, and Alcherio Martinoli. Accommodation of NLOS for ultra-wideband TDoA localization in single- and multi-robot systems. *International Conference on Indoor Positioning and Indoor Navigation (IPIN)*, 2011.

[16] J. Tiemann, F. Eckermann, and C. Wietfeld. ATLAS - an open-source TDOA-based Ultra-wideband localization system. In *Proc. of the International Conference on Indoor Positioning and Indoor Navigation (IPIN)*, pages 1–6, 2016.

[17] Karol Hausman, James Preiss, Gaurav S. Sukhatme, and Stephan Weiss. Observability-Aware Trajectory Optimization for Self-Calibration With Application to UAVs. *IEEE Robotics and Automation Letters*, 2(3):1770–1777, 2017.

[18] Robert Hermann and Arthur J Krener. Nonlinear Controllability and Observability. *IEEE Transactions on Automatic Control*, (5), 1977.

[19] Alberto Isidori, M. Thoma, E. D. Sontag, B. W. Dickinson, A. Fettweis, J. L. Massey, and J. W. Modestino. *Nonlinear Control Systems*. Springer-Verlag, Berlin, Heidelberg, 3rd edition, 1995.

[20] Matteo Ridolfi, Samuel van de Velde, Heidi Steendam, and Eli De Poorter. Analysis of the scalability of UWB indoor localization solutions for high user densities. *Sensors (Switzerland)*, 18(6), 2018.

[21] Stergios I. Roumeliotis, Gaurav S. Sukhatme, and George A. Bekey. Circumventing dynamic modeling: evaluation of the error-state kalman filter applied to mobile robot localization. In *Proc. of the IEEE International Conference on Robotics and Automation (ICRA)*, pages 1656–1663 vol.2, 1999.

[22] Joan Sola. Quaternion kinematics for the error-state kalman filter. *arXiv preprint arXiv:1711.02508*, 2017.